A numerical study of capillary and viscous drainage in porous media

Eyvind Aker

A thesis in partial fulfillment
of the requirements for the
doctoral degree

Doktor ingeniør

Department of Physics
Norwegian University of Science and Technology
Trondheim, Norway

December 1999

Abstract

This work concentrates on the flow properties when one fluid displaces another fluid in a network of pores and throats. We consider the scale where individual pores enter the description and we use a network model to simulate the displacement process. The network model, representing the pores and the throats in the porous medium, consists of a square lattice of cylindrical tubes.

Network models together with experimental work on real porous systems, have been successful in describing important properties of the fluid-fluid displacement. In this thesis we study the interplay between the pressure build up in the fluids and the displacement structure during drainage. Drainage is when a nonwetting fluid displaces a wetting fluid in porous media.

We have found that our network model properly describes the burst dynamics and the pressure buildup due to capillary and viscous forces in the displacements. With respect to the local capillary pressures of menisci in the network, we model the tubes as if they were hourglass shaped. This has shown to make the model closer to the dynamics of real displacements in porous media. There is also good correspondence between the simulated temporal evolution of the fluid pressures and earlier results from experiments and simulations in slow drainage.

We have used the network model to study the stabilization mechanisms when a stable front develops. We consider two-dimensional horizontal displacements where the viscous forces stabilize the front and gravity might be neglected. In particular, we have calculated the pressure difference between the fluids, that is the capillary pressure, along the invasion front. We find that the capillary pressure between two points along the front varies almost linearly as function of height separation in the direction of the displacement. This is quite surprising since the viscous force field is expected to be inhomogeneous due to the trapping of wetting fluid and to the fractal displacement structure.

We present an alternative view on the displacement process based on the observation that nonwetting fluid flows in separate strands (paths) along the front were wetting fluid is displaced. We show that the strands are loopless because wetting fluid may be trapped in single tubes surrounded by nonwetting fluid. By using the alternative view we, present arguments about the pressure behavior in the front. The arguments are supported by numerical results, and we also show that they might influence the scaling relation between the front width and the injection rate. As a consequence of our findings, we conclude that earlier suggested theories which do not include the effect of nonwetting fluid flowing in strands, are not compatible with drainage when strands dominate the displacement process.

Preface

The work presented in this thesis was partly performed at the group of Theoretical Physics at the Department of Physics, Norwegian University of Science and Technology (NTNU) in Trondheim and at the group of Condense Matter at the Department of Physics, University of Oslo (UiO). The project was initiated during my period as a master student at UiO. After graduating in 1997, I continued the project by financial support from the Research Council of Norway (NFR) through a "SUP" program at NTNU, until the end of 1999.

My sincere thanks go to my primary supervisors prof. Alex Hansen (NTNU) and prof. Knut Jørgen Måløy (UiO). I want to thank them for the time they have spent with me, their enthusiasm for the project, and the discussions we have had. Both of them have guided me gently through problems I have encountered and encouraged me to observe the physics in sometimes quite messy results.

When visiting Trondheim, it has been very inspiring to stay at the group of Theoretical Physics at NTNU. The "White House", which is the resort of the theoretical physicists at Gløshaugen, has an unique atmosphere and I want to thank all the people there for their kindness.

In Trondheim, prof. Rune Holt, has introduced me to petroleum related rock mechanics through courses and by visits at IKU (now Sintef Petroleum Research). Even though there has not been time to closer collaboration, I am thankful for learning about the issues in this field.

Inge Frette, a former master student at the group of Condense Matter, UiO, has performed the experiments that are presented in Paper 5. The experiments he has executed have been very valuable, and my last thank goes to him for letting me use his results.

Contents

1 Introduction

This thesis is about pore-scale numerical simulations of drainage displacements in two-dimensional (2D) porous media. The papers forming the main part of this thesis, all report and discuss the results obtained from the simulations as well as describe the simulation model that was used.

Two-phase displacements in porous media have received much attention during the last two decades. In modern physics, the process is of great interest due to the variety of structures obtained when changing the fluid properties like wettability, interfacial tension, viscosities and displacement rate. The different structures obtained have been organized into three flow regimes: viscous fingering [1,2], stable displacement [3], and capillary fingering [4–6]. Viscous fingering is characterized by an unstable front of fingers that is generated when nonwetting and less viscous fluid is displacing wetting and more viscous fluid at relative high injection rate. The fingering structure is found to be fractal with fractal dimension $D = 1.62$ [1,2]. Stable displacement is named after the relative flat and stable front that generates when a nonwetting and more viscous fluid displaces a wetting and less viscous fluid at relative high injection rate. The last scenario, capillary fingering, is obtained when a nonwetting fluid very slowly displaces a wetting fluid. At sufficiently low injection rate the invasion fluid generates a pattern similar to the cluster formed by invasion percolation [4, 7–9]. The displacement is now solely controlled by the capillary pressure, that is the pressure difference between the two fluids across a meniscus in a pore.

Fluid flow in porous media has also been intensively studied because of important applications in a wide range of different technologies. The most important areas that to a great extent depend on properties of fluid flow in porous media, are oil recovery and hydrology. In oil recovery, petroleum engineers are continuously devolving improved techniques to increase the amount of oil they are able to achieve from the oil reservoirs. In hydrology, the on important concern is often to avoid pollution of ground water from human activity.

1.1 Background and motivation

The simulation model used in this thesis is developed to study the dynamics of the temporal evolution of the fluid pressures when a nonwetting fluid displaces a wetting fluid at constant injection rate. With the model we study the pressure in the fluids caused by the viscous forces as well as the capillary forces due to the menisci in the pores. The model porous medium consists of a tube network where the tubes are connected together to form a square lattice.

Numerical simulations of fluid flow in porous media using a network of tubes was first proposed by Fatt [10] in 1956. Since then a large number of publications related to network models and pore-scale displacements have appeared in the literature [1,3,11–23]. Often mentioned is the classic work of Lenormand *et al.* [3] who were the first to systematically classify the displacement structures into the three flow regimes: viscous fingering, stable displacement and capillary fingering. Their network model consisted of pores and throats, situated

respectively at the sites and bonds of a regular 2D square lattice. The pores were spherical and represented the porosity of the network while the throats had resistance to flow but no volume. Each throat was assigned a capillary threshold pressure P_c, and nonwetting fluid was only allowed to enter a throat if the pressure drop across the throat exceeded P_c. The nonwetting fluid invaded the network by completely filling one pore each time step, and menisci between the nonwetting and wetting fluids in the throats were only allowed to move in the forward direction. It is obvious that Lenormand *et al.* did seriously simplifications compared to real porous networks. However, they were able to run systems of typically 100×100 nodes which were an order of magnitude larger than comparable work [11] at that time.

A couple of years before Lenormand *et al.* presented their network model, Dias and Payatakes [12] formulated a model based on throats (tubes) that had sinusoidal shape. They let the capillary pressure change when a meniscus invade a tube, and typically 10 steps were necessary to solve the motion of a meniscus moving through a tube. As the reader will observe later in this thesis, the idea of Dias and Payatakes with respect to the capillary pressure, is similar to the approach in our network model.

It appears that most network models have been used to study statistical properties of the displacement structures or to calculate macroscopic properties like fluid saturations and relative permeabilities. Some have also been used to calculate capillary pressure curves as function of fluid saturation which often is used as input data in reservoir simulations for the oil industry. As far as the author know, it is only van der Marck *et al.* [21] that present a network model simulating the pressure buildup in the fluids, similar to what our model does. They conclude that the simulated pressure is comparable to experimental results when viscosity matched fluids are used, but that there is room for improvement when the viscosity contrast between the fluids is large. Their model is an improved version of the network model developed by Lenormand *et al.* .

There have also been several attempts to simulate the displacement process by using different types of growth algorithms. In 1983 Wilkinson and Willemsen [9] formulated a new form of percolation theory, invasion percolation (IP), that exactly corresponds to slow drainage. In 1984 Paterson [24] was the first to discover the remarkable parallels between diffusion-limited aggregation (DLA) [25] and viscous fingering. He also showed similarities between anti-DLA and stable displacement. The disadvantage with the growth algorithms is that they do not contain any physical time and they have so far not been suitable to study the cross over between the different flow regimes. However, attempts have been made to use DLA and IP to study dynamics of viscous fingering [26] and slow drainage [27, 28], respectively.

In slow drainage it is observed that the invasion of nonwetting fluid occurs in a series of bursts accompanied by sudden negative drops in the pressure called Haines jumps [27–29] (see Fig. 1). This type of dynamics is very important for the temporal evolution of the pressure during drainage, and in most network models the effect is neglected. Consequently, few network models have been used to study the interplay between fluid pressures and displacement structures, and

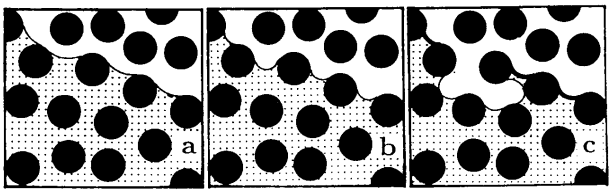

Figure 1: Nonwetting fluid (white) invades a 2D porous medium initially filled with wetting fluid (shaded). As the nonwetting fluid is pumped into the system the menisci move into narrower parts of the pore necks and the capillary pressure increases. During a burst the invading fluid covers new pores and the neighboring menisci readjust back to larger radii and the capillary pressure decreases everywhere [27].

many questions addressing this topic are still open. We will try to answer some of them in this thesis, by making a model whose properties are closer to those of real porous media. To model the burst dynamics, we have been motivated by the hourglass shaped pore necks in Fig. 1. As a result we let the tubes in our network model behave as if they were hourglass shaped with respect to the capillary pressure. Thus, the capillary pressure of a meniscus starts at zero when the meniscus enters the tube and increases towards a maximum value at the middle of the tube where the tube is most narrow, before the capillary pressure decreases to zero again when the meniscus leave the tube.

The advantage of the above approach is a network model that reproduces the burst dynamics and the corresponding pressure evolution. We are also able to study in details the capillary pressure of each menisci along the front as they move through the network. Similar measurements can hardly be done experimentally, and our numerical results concerning the capillary pressure, have given new insight about the displacement process. In particular, we have found that the capillary pressure between two points along the front varies almost linearly as function of height separation in the direction of the displacement. The numerical results support theoretical arguments taking into account the evidence that nonwetting fluid displaces wetting fluid in separate strands. The arguments we present differ from earlier suggested views [30–33] that do not include the effect of nonwetting fluid flowing in strands. Therefore, we conclude that earlier views are incompatible with drainage when nonwetting strands are important.

Unfortunately, the detailed modeling of the moving menisci and their capillary pressures makes the model computationally heavy and reduces the system size that is attainable within feasible amount of CPU time.

1.2 Organization of the introductory sections

The following sections briefly discuss the main results from the papers that are included at the end of this thesis. Section 2 presents the network model which is published in Paper 1. Section 3 discusses the evolution of the pressure

during drainage according to the results in Paper 2. This section also contains work on the burst dynamics due to Paper 3. Section 4 presents simulation results and theoretical arguments about stabilization mechanisms of the front during drainage, and the section is supposed to cover Papers 4 and 5. At the end, Section 5 summaries the most important results and makes suggestions on further work.

2 Simulation model

The network model is thoroughly discussed in Paper 1, and it has also been presented briefly in Papers 2–5. Therefore, only its main features are described in this section.

The porous medium is constructed upon a square lattice oriented at 45° to the horizontal where the distance between each intersection in the lattice is of unit length. In Paper 1 and 2 we put a cylindrical tube of length d and radii r between each intersection in the lattice. The disorder in the system is introduced by assigning different radii to the tubes. The radii are chosen at random from the interval $[\lambda_1 d, \lambda_2 d]$ where $0 \leq \lambda_1 < \lambda_2 \leq 1$. The tubes represent the porosity of the system and they are connected together at the intersections (nodes) having no volume.

In Papers 3–5 we have in addition to above lattice, made a distorted square lattice of tubes. The distorted lattice is constructed by drawing circles of radius λ around each intersection. To avoid overlapping circles we chose λ in the interval $0 \leq \lambda \leq 1/2$. A node without volume is placed at random in each circle and the nodes inside the nearest neighbor circles are connected by cylindrical tubes. Thus, the disorder in the system is introduced by the random position of the nodes resulting in different lengths d of the tubes. The radii of the tubes are given by $r = d/2\alpha$ where α is the aspect ratio between the tube length and its radius. The reason for making a distorted lattice of tubes is to get closer to a real pore-throat geometry as shown in Fig. 1 (see Paper 5 for further details).

Figure 2 shows an example of a displacement structure that is obtained from one simulation. The nonwetting fluid (black) of viscosity μ_{nw} is injected along the inlet and displaces the wetting fluid (grey) of viscosity μ_w. The fluids flow from the bottom to the top of the lattice, and there are periodical boundary conditions in the orthogonal direction. We assume the fluids are immiscible and incompressible.

A meniscus is located in the tubes where nonwetting and wetting fluids meet. The capillary pressure p_c of a meniscus in a cylindrical tube of radius r is given by Young-Lapace law like

$$p_c = \frac{2\gamma}{r} \cos\theta, \tag{1}$$

under the assumption that the principal radii of the curvature of the meniscus are equal to the radius of the tube. θ denotes the wetting angle between the cylinder wall and the wetting fluid, i.e. $0° \leq \theta < 90°$ in drainage.

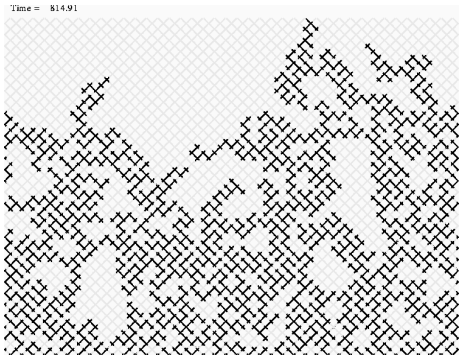

Figure 2: Example of a displacement structure from one simulation. The nonwetting fluid (black) is injected from below and displaces the wetting fluid (grey) that escapes along the top row.

In the network model we treat the tubes as if they were hourglass shaped with respect to the capillary pressure. Therefore, we let the capillary pressure depend on where the meniscus is situated in the tube. In stead of Eq. (1) we let p_c of a meniscus vary in the following way:

$$p_c = \frac{2\gamma}{r}\left[1 - \cos(2\pi\tfrac{x}{d})\right]. \tag{2}$$

Here we assume that the wetting fluid perfectly wets the medium, i.e. $\theta = 0$. In the above relation x denotes the position of the meniscus in the tube ($0 \leq x \leq d$), giving that $p_c = 0$ at the entrance and the exit of the tube and reaches a maximum of $4\gamma/r$ in the middle of the tube ($x = d/2$). Practically, the wetting angle of a meniscus and thereby its capillary pressure may generally be different depending on whether the meniscus retires from or invades the tube. To avoid numerical complications this effect is neglected in the present model.

We solve the volume flux through each tube by using Hagen-Poiseuille flow for cylindrical tubes and Washburn's approximation [34] for menisci under motion. Let q_{ij} denote the volume flux through the tube from the ith to the jth node, then we have

$$q_{ij} = -\frac{\sigma_{ij}k_{ij}}{\mu_{ij}}\frac{1}{d_{ij}}(\Delta p_{ij} - p_{c,ij}). \tag{3}$$

Here k_{ij} is the permeability of the tube ($r_{ij}^2/8$) and σ_{ij} is the cross section (πr_{ij}^2) of the tube. μ_{ij} denotes the effective viscosity, that is the sum of the volume fractions of each fluid inside the tube multiplied by their respective viscosities. The pressure drop across the tube is $\Delta p_{ij} = p_j - p_i$, where p_i and p_j is the pressures at node i and j, respectively. The capillary pressure $p_{c,ij}$ is the sum of the capillary pressures of each menisci [given by Eq. (2)] that are present inside the tube. A tube partially filled with both liquids is allowed to contain at maximum two menisci. For a tube without menisci, $p_{c,ij} = 0$. We only consider horizontal flow, and therefore we neglect gravity.

We have conservation of volume flux at each node giving

$$\sum_j q_{ij} = 0. \tag{4}$$

The summation on j runs over the nearest neighbor nodes to the ith node while i runs over all nodes that do not belong to the top or bottom rows, that is, the internal nodes. Eqs. (3) and (4) constitute a set of linear equations which we solve for the nodal pressures p_i, with the constraint that the pressures at the nodes belonging to the upper and lower rows are kept fixed. The set of equations is solved by using the Conjugate Gradient method [35].

In the simulations we impose the injection rate Q, therefore we have to find the pressure across the lattice ΔP, that corresponds to the given Q. Having found ΔP we use this pressure to calculate the correct p_i's. In short, we find ΔP by considering the relation

$$Q = A\Delta P + B. \tag{5}$$

The first part of Eq. (5) results from Darcy's law for single phase flow through porous media. The second part comes from the capillary pressure between the two fluids (i.e. $B = 0$ if no menisci are present in the network). Eq. (5) has two unknowns, A and B, which we calculate by solving Eq. (4) twice for two different applied pressures $\Delta P'$ and $\Delta P''$, across the lattice. From those two solutions we find the corresponding injection rates Q' and Q''. Inserting Q', Q'', $\Delta P'$, and $\Delta P''$ into Eq. (5) results in two equations which we solve for A and B. Finally, we find the correct pressure due to the imposed Q by rewriting Eq. (5), giving $\Delta P = (Q - B)/A$. See Papers 1 and 2 for further details on how p_i is calculated after ΔP is found.

In the literature different methods have been suggested to obtain a solution where the injection rate is held fixed [3,12,21]. However, it appears that none of them solve the contribution to the pressure due to viscous and capillary forces separately. In Eq. (5) the capillary contribution to the pressure is $-B/A$ and the viscous amount is Q/A. This evidence is thoroughly discussed in Paper 2 and summarized in Sec. 3.

Given the correct solution of p_i we calculate the volume flux q_{ij} through each tube in the lattice, using Eq. (3). Having found the q_{ij}'s we define a time step Δt such that every meniscus is allowed to travel at most a maximum step length $\Delta x_{\max}$ during that time step. Each meniscus is moved a distance $(q_{ij}/\sigma_{ij})\Delta t$ and the total time lapse is recorded before the nodal pressures p_i, are solved for the new fluid configuration. Menisci that are moved out of a tube during a time step are spread into neighboring tubes as described in Papers 1 and 2.

Numerical simulations show that in order to simulate the capillary pressure variations when menisci pass through the "hourglass shaped" tubes we must chose $\Delta x \leq 0.1d$ where d is the tube length. In most of our simulations $\Delta x = 0.1d$, giving that at least 10 steps must be taken to move a meniscus from the inlet to the outlet of a tube. This makes the model computationally heavy due

to an enormous amount of time steps, typically 10^5, that is required before the nonwetting fluid penetrates a network of 40×60 nodes.

Most network models treat the tubes as if they where straight and let the nonwetting fluid completely invade one pore or throat during every time step. Consequently, the total number of time steps is reduced to the number of tubes that the nonwetting fluid invades. In a network of 40×60 nodes this is about 10^3 tubes which should be compared to the 10^5 time steps that are required in our model. This is the main reason why we are limited to rather small system sizes of 25×35 and 40×60 nodes.

3 Temporal evolution of fluid pressure

In Paper 2 we discuss the temporal evolution of the pressure due to capillary and viscous forces at various injection rates and fluid viscosities. The main results from that paper is summarized in Sec. 3.1, while Sec. 3.2 provides a little about burst dynamics due to the results in Paper 3.

To characterize the different fluid properties used in the simulations, we use the capillary number C_a and the viscosity ratio M. The capillary number indicates the ratio between viscous and capillary forces and in the simulations it is defined as

$$C_a \equiv \frac{Q\mu}{\Sigma\gamma}. \tag{6}$$

Here Q is the injection rate of the nonwetting fluid, μ is the maximum viscosity of the nonwetting and wetting fluid, Σ is the cross section of the inlet and γ is the fluid-fluid interface tension.

The viscosity ratio M, is defined as

$$M \equiv \frac{\mu_{nw}}{\mu_w}, \tag{7}$$

where μ_{nw} and μ_w is the viscosity of the invading nonwetting fluid and the defending wetting fluid, respectively.

3.1 Interplay: pressure buildup and trapped fluid

The pressure across the system is found from Eq. (5) giving

$$\Delta P = \frac{Q}{A} + P_{cg}, \tag{8}$$

where $P_{cg} \equiv -B/A$ defines the global capillary pressure of the system. As will become clear below, P_{cg} contains the capillary pressures of the menisci surrounding the trapped wetting fluid (cluster menisci) and the capillary pressures of the menisci along the invasion front (front menisci).

Figure 3 shows the simulated pressures ΔP and P_{cg} during drainage at $C_a = 4.6 \times 10^{-3}$ and $M = 100$. The front width was observed to stabilize after some time t_s, and a typical compact pattern of clusters of wetting fluid

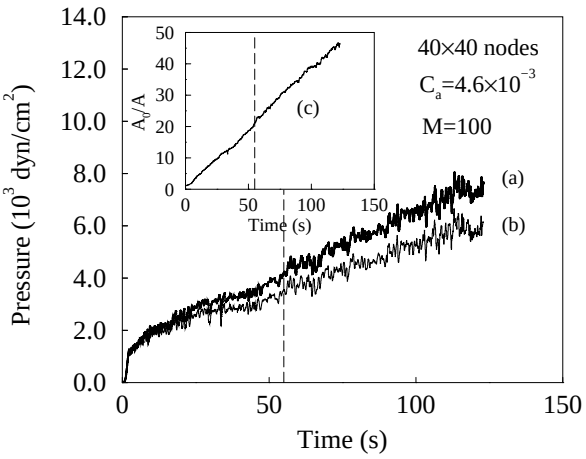

Figure 3: ΔP (a), P_{cg} (b), and A_0/A (c) as function of injection time. $C_a = 4.6\times10^{-3}$ and $M = 100$. The vertical dashed line is drawn at the saturation time, t_s.

developed behind the front. From Fig. 3 we observe that both ΔP and P_{cg} increases as the more viscous fluid is pumped into the system. When $t > t_s$ they even tend to increase linearly as function of time.

The driving mechanism in the displacement is the pressure gradient between the inlet and the front causing a viscous drag on the trapped clusters. At moderate injection rates these clusters are immobile, thus the viscous drag is balanced by capillary forces along the interface of the cluster. On average the sum of the capillary forces from each cluster contributes to P_{cg} by a certain amount making P_{cg} proportional to the number of clusters behind the front. After the front has saturated with fully developed clusters behind ($t > t_s$), the number of clusters are expected to increase linearly with the amount of injected fluid. Since the injection rate is held fixed we recognize that P_{cg} must increase linearly as function of time. The argument does not apply when $t < t_s$, due to the fractal development of the front before saturation.

In Fig. 3 we have also plotted A_0/A which is the normalized difference between ΔP and P_{cg} [see Eq. (8)]. A_0 is equal to the proportionality factor between Q and ΔP when only one phase flows through the lattice (i.e. $P_{cg} = 0$). We observe that A_0/A tends to increase linearly as function of time when $t > t_s$. From Eq. (5) we interpret A as the total conductance of the lattice, and the reciprocal of that is the total resistance. The total resistance depends on the fluid configuration and the geometry of the network. Locally, the fluid configuration changes as nonwetting fluid invades the system, however, the linear behavior of A_0/A indicates that the overall displacement structure is statistically invariant with respect to the injection time. That means, after the front has saturated ($t > t_s$) the displacement structure might be assigned a constant resistance per unit length.

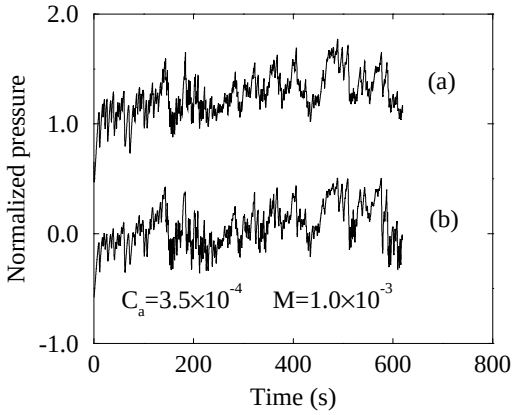

Figure 4: P_{cf} (a) and P_{cg} (b) as function of injection time at $C_a = 3.5\times10^{-4}$ and $M = 1.0\times10^{-3}$. To avoid overlapping curves P_{cg} was subtracted by 1000 dyn/cm^2 before it was normalized.

In the special case when $M = 1$ (viscosity matched fluids) the total resistance, $1/A$, was found to be constant independent of the injection rate or displacement structure. This somewhat surprising result might be explained by the following consideration. When $M = 1$ the effective viscosity μ_{ij}, of each tube is independent of the amount of wetting and nonwetting fluid that occupies the tube. Hence, each tube has a constant conductivity of k_{ij}/μ_{ij} giving a constant total resistance of the network.

At low C_a we approach the regime of capillary fingering and the viscous drag on the clusters becomes negligible. Hence, P_{cg} is no longer a linear function of the injection time, but reduces to that describing the capillary pressure along the front. This is observed in Fig. 4 where we compare P_{cg} with the calculated average capillary pressure along the front, P_{cf}. In the simulations, P_{cf} is calculated by taking the mean of the capillary pressures of the front menisci. From the figure we see that $P_{cg} \simeq P_{cf}$, as expected. The big jumps in the pressure functions in Fig. 4 are caused by the capillary pressure variations of menisci passing through the "hourglass" shaped tubes. The negative jumps are identified as bursts where the invading fluid proceeds abruptly [27,29] (see also Sec. 3.2 for further details).

From the above discussion we conclude that the behavior of P_{cg} at large times ($t > t_s$) may be formulated as

$$P_{cg} = \Delta_{mc} h + P_{mf}, \tag{9}$$

where Δ_{mc} is the proportionality factor between P_{cg} and h due to the viscous drag on the clusters, and P_{mf} is the capillary variations when the invasion front covers new tubes. h denotes the average front position after the front has saturated, i.e. $h_s < h < L$, where h_s is the average front position at t_s and L is

the length of the system. Since the injection rate is held fixed, h is proportional to the injection time t. In the limit of very low injection rates, $\Delta_{mc} \to 0$.

When the average front position has reached the outlet, i.e. $h = L$ in Eq. (9), only invading fluid flows through the system and $P_{mf} = 0$. In this limit Darcy's law applied on the nonwetting phase gives $U = (K_e/\mu_{nw})(\Delta P/L)$, where K_e is the effective permeability of the nonwetting phase. From Eqs. (8) and (9) we find that $\Delta P = Q/A + \Delta_{cm} L$, which inserted into Darcy's law gives

$$K_e = \frac{\mu_{nw}}{1/\sigma_T + \Delta_{mc}/U}. \tag{10}$$

Here $\sigma_T \equiv AL/\Sigma$ denotes the total conductivity of the lattice. Thus, we might consider the effective permeability of the nonwetting phase as a function of the conductivity of the lattice and an additional term due to the viscous drag on the clusters (Δ_{mc}/U). Note that the U dependency in Eq. (10) only indicates changes in Δ_{mc} between displacements executed at different injection rates. The behavior when the flow rate changes during a given displacement is not discussed here.

3.2 Burst dynamics

In invasion percolation (IP) [36] where each site is assigned a random number f, an *ideal* burst is defined as the connected structure that is invaded following one root site of random number f_0 along the invasion front. All the sites in the burst have random numbers smaller than f_0, and the burst stops when $f > f_0$ is the random number of the next site to be invaded [37]. The size of a burst is the number of sites s in the connected structure included the root site.

The distribution of burst sizes $N(s)$ has been found to obey the scaling law [38, 39]

$$N(s) \propto s^{-\tau'} g(s^{\sigma}(f_0 - f_c)). \tag{11}$$

Here f_c is the percolation threshold of the system and $g(x)$ is some scaling function which decays exponentially when $x \gg 1$ and is a constant when $x \to 0$. τ' is related to percolation exponents like $\tau' = 1 + D_f/D - 1/(D\nu)$ [39] where D_f and D is the fractal dimension of the front and the mass of the percolation cluster, respectively. D_f depends on the definition of the front, that is, D_f equals D_e for external perimeter growth zone [36, 40] and D_h for hull perimeter growth zone [36, 41]. ν is the correlation length exponent in percolation theory and $\sigma = 1/(\nu D)$ [36].

In 1995 Maslov [42] deduced a scaling relation for the hierarchical burst size distribution by integrating Eq. (11) over all f_0 in the interval $[0, f_c]$. Thus, the hierarchical burst size distribution contains all ideal bursts including the hierarchical smaller ones that might be within each ideal burst (see Fig. 5). Let $N_{\text{all}}(s)$ denote the hierarchical burst size distribution, then according to Maslov [42]

$$N_{\text{all}}(s) \propto s^{-\tau_{\text{all}}}, \tag{12}$$

where $\tau_{\text{all}} = 2$.

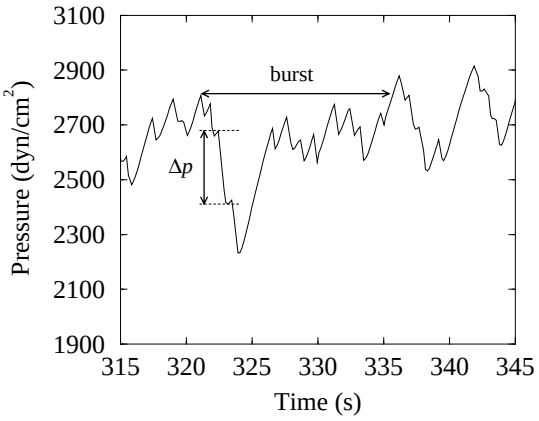

Figure 5: The pressure as function of injection time for one simulation at low C_a in a narrow time interval. The horizontal line defines the valley of a single burst. Note that a burst may contain a hierarchical structure of smaller bursts within the valley. The vertical line indicates the size of a local pressure jump Δp inside the valley.

In Ref. [28], τ' and τ_{all} were estimated for simulations and experiments in slow drainage. The simulation model used in [28] was a modified IP algorithm designed to study the burst dynamics of capillary fingering. To check that the burst dynamics are properly modeled in our network model we calculate τ' and τ_{all} from simulations performed in the limit of low injection rates. In addition, we compute the hierarchical burst size distribution at higher injection rates to observe a possible rate dependency of τ_{all}. Below a summary of the results is provided.

In the simulations a burst starts where the pressure drops suddenly, due to an unstable meniscus, and stops where the pressure has raised to a value above the pressure that initiated the burst. Thus, a burst may consist of a large pressure valley containing a hierarchical structure of smaller bursts inside, as indicated in Fig. 5. From the simulations we could have calculated the geometrical size of the region being invaded during a burst. That would correspond to the burst size s in Eqs. (11) and (12). However, we want to compare our results to experimental work in [28] where the geometrical size is hard to measure. Therefore, we calculate the burst sizes in analogy to definitions in [28].

According to [28] we define the burst size as the sum of the pressure jumps inside the valley of the burst (see Fig. 5). We call the sum of the pressure jumps the valley size given as $\chi \equiv \sum_i \Delta p_i$. Here the index i runs over all the pressure jumps Δp_i inside the valley. In order to calculate the valley sizes at large C_a we subtract the average drift in the pressure function due to viscous forces, such that the pressure becomes a function fluctuating around some mean pressure. We assume that the valley size χ, is proportional to the geometrical size of the region being invaded during a burst [28], and therefore χ becomes

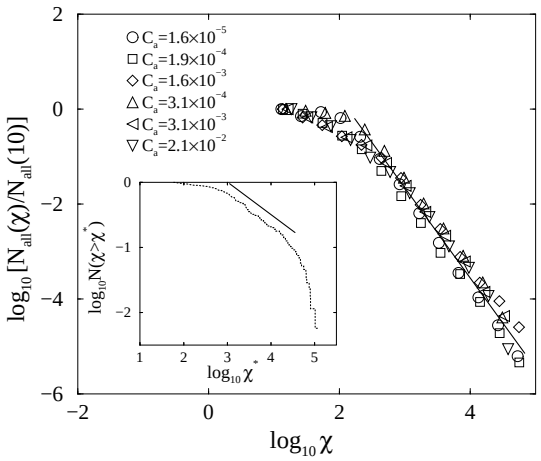

Figure 6: The hierarchical valley size distributions $N_{\rm all}(\chi)$, for six simulations between low and high C_a with $M = 1$ ($\circ, \square, \diamond$) and $M = 100$ ($\triangle, \triangleleft, \triangledown$). The slope of the solid line is -1.9. *Inset*: The cumulative valley size distribution $N(\chi > \chi^*)$, for bursts that start in a narrow pressure strip for the simulation performed at $C_a = 1.6 \times 10^{-5}$ and $M = 1$. The slope of the solid line is -0.5.

roughly proportional to s.

In Fig. 6 we have plotted the hierarchical valley size distribution $N_{\rm all}(\chi)$, for six simulations between low and high C_a with $M = 1$ and 100 on a lattice of 40×60 and 25×35 nodes, respectively. Since we assume that $\chi \propto s$, $N_{\rm all}(\chi)$ corresponds to $N_{\rm all}(s)$ in Eq. (12). The slope of the solid line in Fig. 6 is -1.9, and we conclude from the simulations that $\tau_{\rm all} = 1.9 \pm 0.1$. At low χ in Fig. 6, typically only one tube has been invaded during the burst and we do not expect the power law to be valid.

Our calculated $\tau_{\rm all}$ is close the theoretical prediction in Eq. (12) and the result of simulations and experiments in [28] at low C_a. We might have introduced some errors when we compare χ with the burst sizes s which may explain why our result deviates a little from the exact value $\tau_{\rm all} = 2$. From Fig. 6 we note that our estimated $\tau_{\rm all}$ does not depend on C_a. Even at high C_a where a flat front generates we find $\tau_{\rm all} = 1.9 \pm 0.1$. In [42] $\tau_{\rm all}$ was pointed out to be super universal for a broad class of self-organized critical models including IP. Our result indicates that the simulated displacement process might belong to the same super universality class even at high injection rates where there is no clear mapping between the displacement process and IP.

In the inset of Fig. 6 we have plotted the cumulative valley size distribution $N(\chi > \chi^*)$ for bursts starting in a narrow strip between 2800 and 3100 dyn/cm^2 where 3100 is the maximum pressure during the displacement. From Eq. (11) we have that $N(s) \propto s^{-\tau'}$, for bursts that start close to the percolation threshold f_c. In our simulations f_c corresponds to the maximum pressure. In the inset

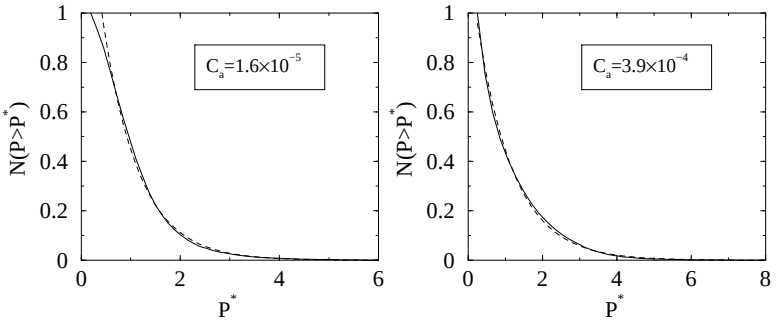

Figure 7: The cumulative pressure jump distribution function $N(P>P^*)$, for simulations performed with viscosity matched fluids ($M = 1$) on a lattice of 40×60 nodes. The dashed lines are fitted exponential functions.

of Fig. 6 we have plotted $N(\chi > \chi^*)$ versus χ^* in a logarithmic plot for one simulation performed at low $C_a = 1.6 \times 10^{-5}$ with viscosity matched fluids on a lattice of 40×60 nodes. If we assume a power law behavior our best estimate is $1 - \tau' = -0.5$ which is indicated by the slope of the solid line in Fig. 6. In [28] simulations and experiments gave $1 - \tau' = -0.45 \pm 0.10$. We need larger system sizes and more simulations to improve our statistics. However, our result seems to be consistent with [28].

We have also calculated the cumulative pressure jump distribution function $N(P > P^*)$ for simulations at various injection rates and viscosity ratios. The pressure $P = \Delta p / \langle \Delta p \rangle$, where $\langle \Delta p \rangle$ is the mean of the pressure jumps Δp (see Fig. 5). In Fig. 7 we have plotted the result for two simulations, one at high and the other at low C_a. Both were performed with viscosity matched fluids on a lattice of 40×60 nodes. The distributions have been fitted to exponentially decreasing functions plotted as dashed lines in Fig. 7. At low C_a we find $N(P > P^*) \propto e^{-1.38P^*}$ which is consistent with the results in [28]. At high C_a the distribution function was fitted to $e^{-1.02P^*}$. The pre-factor in the exponent of the exponential function seems to change systematically from about 1.4 to 1.0 as C_a increases. Similar results were obtained from simulations performed with $M = 100$ on a lattice of 25×35 nodes.

From Figs. 6 and 7 we conclude that the results of our network simulations are in agreement with experiments and simulations performed in [28] at slow drainage. This supports the evidence that the burst dynamics are well described by our network model.

4 Stabilization of drainage displacements

Papers 4 and 5 discuss the stabilization mechanisms of drainage displacements due to viscous forces and present new theoretical arguments about the pressure

behavior along the front. Below, a briefly review of earlier work on stabilization of drainage displacements is provided, before the arguments and the supporting numerical results are presented in Sec. 4.1. At the end, Sec. 4.2 investigates the general validity of the arguments and raises important questions going beyond the discussion in Sec. 4.1.

When the displacements are oriented out of the horizontal plane, gravity acting on the system, may stabilize the front due to density differences between the fluids. Several authors [30, 43–45] have confirmed, by experiments and simulations, that the saturated front width w_s scales with the strength of gravity like $w_s \propto {B_o}^{-\nu/(1+\nu)}$. Here B_o (Bond number) is the ratio between gravitational and capillary forces, given by $B_o = \Delta\rho g a^2/\gamma$, where $\Delta\rho$ is the density difference between the fluids, g the acceleration due to gravity, a the average pore size, and γ the fluid-fluid interface tension. Furthermore, ν denotes the correlation length exponent in percolation. The above scaling relation may be deduced from IP by applying a gradient proportional to $-B_o$ to the random numbers of the sites in the percolation lattice. This will cause the invasion front to stabilize [30, 44, 46].

A similar consensus concerning the stabilization mechanisms when the displacements are within the horizontal plan has not yet been reached. Here viscous forces replace gravitational forces, and in the literature there exist different suggestions about the scaling of w_s as function of C_a. The capillary number C_a is the ratio between viscous and capillary forces according to the definition in Sec. 3. In 3D, where trapping of wetting fluid is assumed to be of little importance, Wilkinson [30] was the first to use percolation to deduce a power law like $w_s \propto {C_a}^{-\alpha}$ where $\alpha = \nu/(1 + t - \beta + \nu)$. Here t and β is the conductivity and order parameter exponent in percolation, respectively. Later, Blunt *et al.* [32] suggested in 3D that $\alpha = \nu/(1 + t + \nu)$. This is identical to the result of Lenormand [31] finding a power law as function of system size for the domain boundary in the C_a–M plane between capillary fingering and stable displacement in 2D porous media.

More recently, Xu *et al.* [33] used a similar approach as Wilkinson and found that the pressure drop ΔP_{nw} across a height difference Δh in the nonwetting phase of the front should scale as $\Delta P_{nw} \propto \Delta h^{t/\nu + d_{\mathrm{E}} - 1 - \beta/\nu}$. Here d_{E} denotes the Euclidean dimension of the space in which the front is embedded, i.e. in our case $d_{\mathrm{E}} = 2$. The pressure drop in the wetting phase ΔP_w, was argued to be linearly dependent on Δh due to the compact phase there. In [32] Blunt *et al.* also suggested a scaling relation for ΔP_{nw}, however, in 3D they found $\Delta P_{nw} \propto \Delta h^{t/\nu+1}$. This is different from the result of Xu *et al.* when $d_{\mathrm{E}} = 3$.

In Sec. 4.1 we present an alternative view on the displacements from those initiated by Wilkinson [30], but include the evidence that nonwetting fluid flows in separate strands. The alternative view leads to another scaling of ΔP_{nw} than the one suggested by Xu *et al.* [33], and we show that it may influence α in the scaling between w_s and C_a.

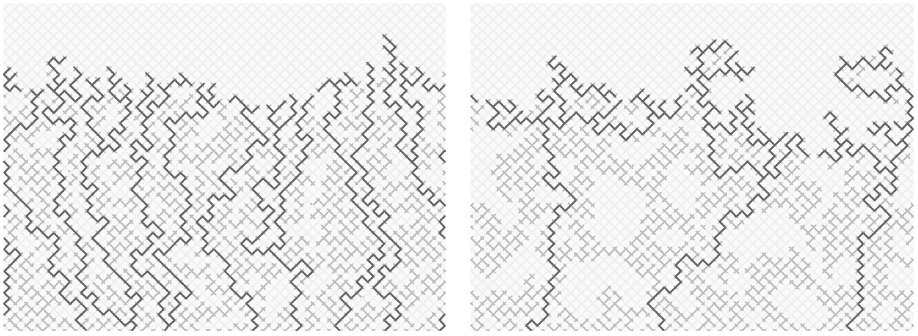

Figure 8: Two displacement structures of simulations at high $C_a = 3.9\times10^{-4}$ (left) and low $C_a = 1.6\times10^{-5}$ (right) before breakthrough of nonwetting fluid. The lattice size is 40×60 nodes and $M = 1$. The nonwetting fluid (dark grey and black) is injected from below and wetting fluid (light grey) flows out along the top row. The black tubes denote the loopless strands where nonwetting fluid flows and the dark grey tubes indicate nonwetting fluid unable to flow (i.e. dead ends) due to trapped regions of wetting fluid. Note the few fluid supplying strands from the inlet to the frontal region at low C_a compared to the case at high C_a.

4.1 Loopless strands

Figure 8 shows two typical displacement structures that were obtained from simulations at low and high C_a on a lattice of 40×60 nodes with $M = 1$. From the figure we observe that the nonwetting fluid (dark grey and black) generates patterns containing no closed loops. That means, following a path of nonwetting fluid will never bring us back to the starting point. The nonwetting fluid also flows in separate loopless strands, indicated as black tubes in Fig. 8. The loopless structures in Fig. 8 are a direct consequence of the evidence that a tube filled with wetting fluid and surrounded on both sides by nonwetting fluid is trapped due to volume conservation of wetting fluid. We note that this evidence may easily be generalized to 3D, and therefore our arguments should apply there too. Similar loopless features were also pointed out in [47] for site-bond IP with trapping and in [48] for a loopless IP algorithm.

From Fig. 8 we may separate the displacement patterns into two parts. One consisting of the frontal region continuously covering new tubes, and the other consisting of the more static structure behind the front. The frontal region is supplied by nonwetting fluid through a set of strands that connect the frontal region to the inlet. When the strands approach the frontal region they are more likely to split. Since we are dealing with a square lattice, a splitting strand may create either two or three new strands. As the strands proceed upwards in Fig. 8, they split repeatedly until the frontal region is completely covered by nonwetting strands.

On IP patterns with trapping [47] and without loops [48, 49] the length l of the minimum path between two points separated an Euclidean distance R scales

like $l \propto R^{D_s}$ where D_s is the fractal dimension of the shortest path. We assume that the displacement patterns of the frontal region for lengths less than the correlation length (in our case w_s) is statistically equal to IP patterns in [47]. Therefore, the length of individual nonwetting strands in the frontal region, is proportional to Δh^{D_s} where Δh is some vertical length less than w_s. If we assume that every tube in the lattice on average has the same mobility (k_{ij}/μ_{ij}), we obtain that the fluid pressure within one strand must drop like Δh^{κ} where $\kappa = D_s$. Let us now consider the effect on the pressure when strands split. If we assume that the strands are straight ($D_s = 1$), then by following a path where strands split would cause the pressure to drop as Δh^{κ} where $\kappa < 1$. This is because the volume fluxes through the new strands must be less than the flux in the strand before it splits, due to volume conservation of nonwetting fluid. From Fig. 8, we note that at high C_a the lengths of individual strands in the frontal region approach the minimum length due to the tubes. Therefore, in this limit finite size effects are expected to cause $D_s \to 1$.

The two results ($\kappa = D_s$ and $\kappa < 1$) predict that the pressure drop in the nonwetting phase of the frontal region, ΔP_{nw}, should scale as $\Delta P_{nw} \propto \Delta h^{\kappa}$ where $\kappa \leq D_s$. In 2D two different values for D_s have been reported: $D_s = 1.22$ [48, 49] for loopless IP patterns growing around a central seed, and $D_s = 1.14$ [47] for the single strand connecting the inlet to the outlet when nonwetting fluid percolates the system. We note that the result in [47] is essentially equal to $D_{\min} = 1.13$ [36, 50], that is the fractal dimension of the minimum path in 2D percolation where loops generally occur. According to Xu *et al.* [33], $\kappa = t/\nu + d_{\mathrm{E}} - 1 - \beta/\nu \approx 1.9$ in 2D where we have inserted $t = 1.3$, $\nu = 4/3$, $\beta = 5/36$, and $d_{\mathrm{E}} = 2$. Thus, our arguments based on the loopless strands of nonwetting fluid are incompatible with the result in [33].

To confirm the above arguments giving $\kappa \leq D_s$, we have calculated the difference in capillary pressure ΔP_c between menisci along the front in the direction of the displacement using our network model. ΔP_c as function of Δh was calculated by taking the mean of the capillary pressure differences between all pairs of menisci separated a vertical distance Δh along the front (see Paper 5 for details). Figure 9 shows ΔP_c as function of Δh for simulations performed at various C_a, M, and system sizes. The left figure shows ΔP_c for simulations performed on systems of 25×35 and 40×60 nodes where $M = 100$ and 1, respectively. We did 10–30 simulations at each C_a to obtain reliable average quantities.

To the right in Fig. 9, we have plotted $\log_{10}(\Delta P_c)$ versus $\log_{10}(\Delta h)$ for simulations performed on four patterns generated at systems of 200×300 nodes by an IP algorithm. In these simulations the tubes in the network model were initially filled with nonwetting and wetting fluid according to the generated IP patterns. The network model was started from this point and ran a limited number of time steps while ΔP_c was recorded. By this way, we were able to study ΔP_c on large systems in the low C_a regime, because we saved the computation time that would have been required if similar displacement patterns should have been generated by the network model. Instead, the patterns were generated by a much faster IP algorithm. To make this method self-consistent we had to assume

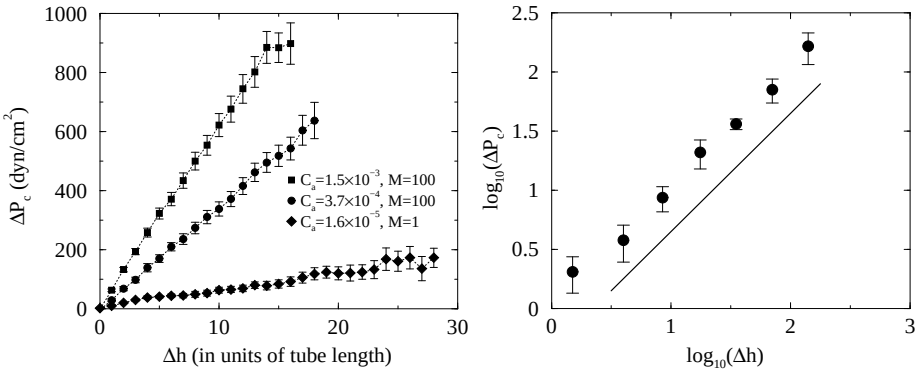

Figure 9: *Left:* ΔP_c as function of Δh for three different C_a's with $M = 100$ and 1 on lattices of 25×35 and 40×60 nodes, respectively. *Right:* $\log_{10}(\Delta P_c)$ as function of $\log_{10}(\Delta h)$ for simulations initiated on IP patterns at $C_a = 9.5 \times 10^{-5}$ and $M = 100$. The slope of the solid line is 1.0.

that the IP patterns were statistically equal to corresponding structures that would have been generated by the network model. See Paper 5 for details about the IP algorithm and how the network model was initiated by the generated patterns.

From the results in Fig. 9 we conclude that ΔP_c increases almost linearly with Δh. Assuming a power law behavior like $\Delta P_c \propto \Delta h^{\kappa}$, our best estimate of the exponent is $\kappa = 1.0 \pm 0.1$. We have also performed simulations on IP patterns at $C_a = 2 \times 10^{-6}$ with $M = 1$ and 100. The results of those are consistent with the plot to the right in Fig. 9. The behavior of ΔP_c is connected to ΔP_{nw} through $\Delta P_c \simeq \Delta P_{nw} - \Delta P_w$. Here ΔP_w is the pressure drop in the wetting phase of the frontal region and varies linearly as function of height Δh. The above relation was suggested in [33] and it is also confirmed by our simulations. Hence, our simulations giving $\kappa \simeq 1.0$ support the arguments finding $\kappa \leq D_s$ in $\Delta P_{nw} \propto \Delta h^{\kappa}$. Therefore, we conclude that earlier proposed theories [30–33] which do not consider the evidence that nonwetting fluid flows in strands, are incompatible with drainage when strands are important.

The evidence that $\kappa \leq D_s$ may influence the exponent α in $w_s \propto {C_a}^{-\alpha}$. Assuming Darcy flow where the pressure drop depends linearly on the injection rate, we conjecture that $\Delta \widehat{P}_c \propto C_a \Delta h^{\kappa}$. Here $\Delta \widehat{P}_c$ denotes the capillary pressure difference over a height Δh when the front is stationary. That means, $\Delta \widehat{P}_c$ excludes situations where nonwetting fluid rapidly invades new tubes due to local instabilities (i.e. bursts). The above conjecture is supported by simulations showing that in the low C_a regime $\Delta \widehat{P}_c \propto C_a \Delta h^{\kappa}$ where $\kappa \simeq 1.0$. Note, that $\Delta \widehat{P}_c \not\propto \Delta P_c$ in Fig. 9 since the latter includes both stable situations and bursts.

At sufficiently low C_a where only the strength of the capillary pressure decides which tube should be invaded or not, we may map the displacement process to percolation giving $\Delta \widehat{P}_c \propto f - f_c \propto \xi^{-1/\nu}$ [30, 44, 46]. Here f is the random

numbers in the percolation lattice, f_c is the critical percolation threshold, and $\xi \propto w_s$ is the correlation length. Combining the above relations for $\Delta\widehat{P}_c$ gives $w_s \propto {C_a}^{-\alpha}$ where $\alpha = \nu/(1+\nu\kappa)$. In 2D $\nu = 4/3$ and by inserting $\kappa = 1.0$ we obtain $\alpha \approx 0.57$. Note that this is different to results suggested in [30, 32, 33] giving $\alpha \approx 0.37$–0.38 in 2D.

At high C_a the nonwetting fluid is found to invade simultaneously everywhere along the front, and consequently the front never reaches a stationary state (see Paper 5). In this limit simulations show a nonlinear dependency between $\Delta\widehat{P}_c$ and C_a. Therefore, in the high C_a regime it is not clear if the above mapping to percolation is valid, and we expect another type of behavior between w_s and C_a.

Frette *et al.* [51] have performed 2D drainage experiments where w_s was measured as function of C_a for viscosity matched fluids ($M = 1$). Their best estimate on the exponent in $w_s \propto {C_a}^{-\alpha}$ was $\alpha = 0.6 \pm 0.2$. This is consistent with the above conjecture ($\alpha = 0.57$), however, corresponding simulations on 40×60 nodes lattices give $\alpha = 0.3 \pm 0.1$ (see Paper 5). The simulations are performed at $C_a \geq 1.0{\times}10^{-5}$ while most of the experiments where done at $C_a \leq 1.0{\times}10^{-5}$. Since the range of the two does not overlap it is difficult to compare the result of the simulations with those of the experiments. However, the change in α from 0.6 to 0.3, might be consistent with a crossover to another behavior at high C_a according to the above discussion. We also note, that for the simulations at $C_a \simeq 1.0{\times}10^{-5}$, the front width approaches the maximum width due to the system size, making it difficult to observe any possible $\alpha \approx 0.57$ regime at low C_a. We emphasize that more simulations on larger systems and at lower C_a are needed before any conclusion on α can be drawn.

4.2 Range of validity

The evidence that the nonwetting fluid displaces the wetting fluid in a set of loopless strands opens new questions about the displacement process. Returning to Fig. 8 it is striking to observe the different patterns of strands at high and low C_a. At low C_a few strands are supplying the frontal region with nonwetting fluid, and the strands split many times before the whole front is covered. At high C_a the horizontal distance between each strand in the static structure is much shorter, and only a few splits are required to cover the front. We conjecture that the average horizontal distance between the fluid suppling strands depends on the front width. However, further investigation of the displacement patterns is required before any conclusions can be drawn.

So far the arguments in Sec. 4.1 only consider displacements where the nonwetting strands contain no loops. A very interesting question that has to be answered is: What happens to κ when different strands in the front connect to generate loops. In ordinary bond or site percolation loops generally occur. Loops are also observed in experiments corresponding to those of Frette *et al.* [51]. In the experiments it is more difficult to trap wetting fluid due to the more complex topology of pores and throats (see Fig. 1). Consequently, loops will more easily generate there, than in the case of a regular square lattice.

Loops might also be created when neighboring menisci along the front overlap and coalesce depending on the wetting properties of the nonwetting fluid [5, 6].

As a first approximation we conjecture that creation of loops will not cause κ to change significantly. Note that in the front the different nonwetting strands connecting to each other to create loops, must at some later time split. Otherwise successive connections will cause the different strands to coalesce into one single strand of nonwetting fluid. Moreover, after the front width has saturated, the number of places where different strands connect must on average be equal to the number of places where strands split. Therefore, we believe that the influence on κ due to connections (i.e. loops) will be compensated by the splits and the overall behavior of κ will remain the same. We emphasize that further simulations and experiments are required to investigate the effect of loops on κ. Hopefully, that will confirm the above conjecture.

According to the discussion in Sec. 4.2, the evidence that the displacement patterns consist of loopless strands may easily be generalized to 3D. Therefore we conjecture that our arguments giving $\kappa \leq D_s$, might be valid in 3D as well. Note also that in 3D it is less probable that different strands meet. Hence, even if they were supposed to connect to create loops, the number of created loops are expected to be few. In 3D the fractal dimension of the shortest path for loopless IP is $D_s = 1.42$ [48] whereas for regular percolation $D_s = 1.34$ [36, 50].

5 Summary and further work

We conclude that our 2D network model properly simulates the temporal evolution of the pressure in the fluids during drainage. We have found that the model reproduces the typical burst dynamics at low injection rates and we have simulated the behavior of the capillary pressure along the front. The latter can hardy be measured experimentally.

Simulations show that the capillary pressure difference ΔP_c between two points along the front varies almost linearly as function of height separation Δh in the direction of the displacement. The numerical result supports arguments based on the observation that nonwetting fluid flows in separate strands where wetting fluid is displaced. From the arguments we find that $\Delta P_c \propto \Delta h^{\kappa}$ where $\kappa \leq D_s$. Here D_s denotes the fractal dimension of the nonwetting strands. It is interesting to observe that despite the small system sizes of our simulations, we are able to use the numerical results to grasp new physics and confirm our arguments.

Several attempts have been made to describe the stabilization mechanisms in drainage due to viscous forces, however, none of them consider the evidence that nonwetting fluid displaces wetting fluid through strands. Therefore, we conclude that earlier suggested theories fail to describe the stabilization of the invasion front when strands dominate the displacements.

According to Sec. 4.2 there are still work to be done about the stabilization mechanisms in drainage. Especially, the indication that the arguments giving $\kappa \leq D_s$ in 2D, might apply in 3D too, should be thoroughly checked. The

effect on κ of possible loops should also be investigated further. Particularly, a closer study of loops being created in drainage experiments, are necessary. Presumably one will find that different strands in the experiments may connect to create loops. However, the overall picture of nonwetting strands that split to cover the front, should remain.

In the literature, different values of D_s in 2D have been reported (see Sec. 4.1), and a closer examination of the fractal dimension of the strands are required in order to find the correct D_s for our problem. It is also of particular interest to develop another numerical scheme of simulations which are able to simulate the displacements on larger lattices in the low C_a regime. Hopefully, this will confirm the conjectured $\alpha = \nu/(1+\nu\kappa)$ in the power law $w_s \propto {C_a}^{-\alpha}$ from Sec. 4.1.

Another issue that the literature contains little information about, is the effect on the displacement patterns when changing the pore size distribution. In [1] the pore size distribution was varied in some experiments and simulations in the regime of viscous fingering. The effect of changing the pore size distribution has also been discussed in connection with the transition from self-similar fractal to faceted growth when varying the wetting angle of the invading fluid [6]. It appears that no one has yet systematically studied the effect of the front width when changing the pore size distribution in drainage displacements.

The network model presented in this thesis only simulates drainage. The imbibition mechanism like film flow is not included and the methods we apply when moving menisci into neighboring tubes are motivated by displacement mechanisms observed in drainage [52] (see Paper 1 for details). A continuation of this project could be to improve the model by including imbibition mechanisms. Still, modeling of the fluid pressures due to capillary and viscous forces during imbibition is an outstanding problem [53].

References

[1] J.-D. Chen and D. Wilkinson, *Phys. Rev. Lett.* **55**, 1892 (1985).

[2] K. J. Måløy, J. Feder, and T. Jøssang, *Phys. Rev. Lett.* **55**, 26881 (1985).

[3] R. Lenormand, E. Touboul, and C. Zarcone, *J. Fluid Mech.* **189**, 165 (1988).

[4] R. Lenormand and C. Zarcone, *Phys. Rev. Lett.* **54**, 2226 (1985).

[5] M. Cieplak and M. O. Robbins, *Phys. Rev. Lett.* **60**, 2042 (1988).

[6] M. Cieplak and M. O. Robbins, *Phys. Rev. B.* **41**, 11508 (1990).

[7] P. G. de Gennes and E. Guyon, *J. Mec. (Paris)* **17**, 403 (1978).

[8] R. Chandler, J. Koplik, K. Lerman, and J. F. Willemsen, *J. Fluid Mech.* **119**, 249 (1982).

[9] D. Wilkinson and J. F. Willemsen, *J. Phys. A* **16**, 3365 (1983).

[10] I. Fatt, *Petroleum Trans. AIME* **207**, 144 (1956).

[11] J. Koplik and T. J. Lasseter, *SPEJ* **22**, 89 (1985).

[12] M. M. Dias and A. C. Payatakes, *J. Fluid Mech.* **164**, 305 (1986).

[13] P. R. King, *J. Phys. A* **20**, L529 (1987).

[14] M. Blunt and P. King, *Phys. Rev. A* **42**, 4780 (1990).

[15] M. Blunt and P. King, *Transp. Porous Media* **6**, 407 (1991).

[16] P. C. Reeves and M. A. Celia, *Water Resour. Res.* **32**, 2345 (1996).

[17] G. N. Constantinides and A. C. Payatakes, *AIChE Journal* **42**, 369 (1996).

[18] E. W. Pereira, W. V. Pinczewski, D. Y. C. Chan, L. Paterson, and P. E. Øren, *Transp. Porous Media* **24**, 167 (1996).

[19] D. H. Fenwick and M. J. Blunt. In *proc. of the SPE Annual Tech. Conf., SPE 38881*, San Antonio, Texas, U.S.A., Oct. 1997.

[20] P. E. Øren, S. Bakke, and O. J. Arntzen. In *proc. of the SPE Annual Tech. Conf., SPE 38880*, San Antonio, Texas, U.S.A., Oct. 1997.

[21] S. C. van der Marck, T. Matsuura, and J. Glas, *Phys. Rev. E* **56**, 5675 (1997).

[22] D. H. Fenwick and M. J. Blunt, *Adv. Water Res.* **21**, 121 (1998).

[23] H. K. Dahle and M. A. Celia, *Comp. Geosci.* **3**, 1 (1999).

[24] L. Paterson, *Phys. Rev. Lett.* **52**, 1621 (1984).

[25] T. A. Witten and L. M. Sander, *Phys. Rev. Lett.* **47**, 1400 (1981).

[26] K. J. Måløy, F. Boger, J. Feder, and T. Jøssang, *Phys. Rev. A* **36**, 318 (1987).

[27] K. J. Måløy, L. Furuberg, J. Feder, and T. Jøssang, *Phys. Rev. Lett.* **68**, 2161 (1992).

[28] L. Furuberg, K. J. Måløy, and J. Feder, *Phys. Rev. E* **53**, 966 (1996).

[29] W. B. Haines, *J. Agr. Sci.* **20**, 97 (1930).

[30] D. Wilkinson, *Phys. Rev. A* **34**, 1380 (1986).

[31] R. Lenormand, *Proc. Roy. Soc. Lond.A* **423**, 159 (1989).

[32] M. Blunt and M. J. King, *Phys. Rev. A* **46**, 7680 (1992).

[33] B. Xu, Y. C. Yortsos, and D. Salin, *Phys. Rev. E* **57**, 739 (1998).

[34] E. W. Washburn, *Phys. Rev.* **17**, 273 (1921).

[35] G. G. Batrouni and A. Hansen, *J. Stat. Phys.* **52**, 747 (1988).

[36] D. Stauffer and A. Aharony. *Introduction to percolation theory.* Taylor & Francis, London, Great Britain, 1992.

[37] S. Roux and E. Guyon, *J. Phys. A: Math. Gen.* **22**, 3693 (1989).

[38] B. Sapoval, M. Rosso, and J. F. Gouyet. In *Fractals' Physical Origin and Properties*, edited by L. Pietronero, Plenum Press, New York, 1989.

[39] N. Martys, M. O. Robbins, and M. Cieplak, *Phys. Rev. B.* **44**, 12294 (1991).

[40] T. Grossman and A. Aharony, *J. Phys. A: Math. Gen.* **20**, L1193 (1987).

[41] R. F. Voss, *J. Phys. A: Math. Gen.* **17**, L373 (1984).

[42] S. Maslov, *Phys. Rev. Lett.* **74**, 562 (1995).

[43] D. Wilkinson, *Phys. Rev. A* **30**, 520 (1984).

[44] A. Birovljev, L. Furuberg, J. Feder, T. Jøssang, K. J. Måløy, and A. Aharony, *Phys. Rev. Lett.* **67**, 584 (1991).

[45] P. Meakin, A. Birovljev, V. Frette, J. Feder, T. Jøssang, K. J. Måløy, and A. Aharony, *Physica A* **191**, 227 (1992).

[46] J.-F. Gouyet, B. Sapoval, and M. Rosso, *Phys. Rev. B* **37**, 1832 (1988).

[47] M. Sahimi, M. Hashemi, and J. Ghassemzadeh, *Physica A* **260**, 231 (1998).

[48] M. Cieplak, A. Maritan, and J. R. Banavar, *Phys. Rev. Lett.* **76**, 3754 (1996).

[49] M. Porto, S. S. Havlin, and B. A., *Phys. Rev. Lett.* **79**, 4060 (1997).

[50] H. J. Herrmann and H. E. Stanley, *J. Phys. A* **21**, L829 (1988).

[51] O. I. Frette, K. J. Måløy, J. Schmittbuhl, and A. Hansen, *Phys. Rev. E.* **55**, 2969 (1997).

[52] R. Lenormand, C. Zarcone, and A. Sarr, *J. Fluid. Mech.* **135**, 337 (1983).

[53] S. C. van der Marck and J. Glas, *Eur. J. Mech., B/Fluids* **16**, 681 (1997).

List of scientific papers

Paper 1: Eyvind Aker, Knut Jørgen Måløy, Alex Hansen and G. George Batrouni: A two-dimensional network simulator for two-phase flow in porous media, *Trans. Porous Media* **32**, 163 (1998)

Paper 2: Eyvind Aker, Knut Jørgen Måløy and Alex Hansen: Simulating temporal evolution of pressure in two-phase flow in porous media, *Phys. Rev. E* **58**, 2217 (1998)

Paper 3: Eyvind Aker, Knut Jørgen Måløy, Alex Hansen and S. Basak: Burst dynamics during drainage displacements in porous media: Simulations and experiments, *submitted to Europhys. Lett.* (1999)

Paper 4: Eyvind Aker, Knut Jørgen Måløy and Alex Hansen: Viscous stabilization of the invasion front in drainage displacement, *submitted to Phys. Rev. Lett.* (1999)

Paper 5: Eyvind Aker, Knut Jørgen Måløy and Alex Hansen: Dynamics of stable viscous displacement in porous media, *submitted to Phys. Rev. E* (1999)